Journal of Biomechanics 85 (2019) 108–117

Contents lists available at ScienceDirect

Journal of Biomechanics

journal homepage: www.elsevier.com/locate/jbiomech
www.JBiomech.com

Characterization and estimation of turbulence-related wall shear stress in patient-specific pulsatile blood flow

Magnus Andersson [a,*], Tino Ebbers [b,c], Matts Karlsson [a,c]

[a] Department of Management and Engineering (IEI), Linköping University, Linköping, Sweden
[b] Department of Medical and Health Sciences (IMH), Linköping University, Linköping, Sweden
[c] Center for Medical Image Science and Visualization (CMIV), Linköping University, Linköping, Sweden

ARTICLE INFO

Article history:
Accepted 8 January 2019

Keywords:
Computational fluid dynamics
Disturbed hemodynamics
Anisotropy invariant map
Aortic coarctation
Near-wall surrogate markers

ABSTRACT

Disturbed, turbulent-like blood flow promotes chaotic wall shear stress (WSS) environments, impairing essential endothelial functions and increasing the susceptibility and progression of vascular diseases. These flow characteristics are today frequently detected at various anatomical, lesion and intervention-related sites, while their role as a pathological determinant is less understood. To present-day, numerous WSS-based descriptors have been proposed to characterize the spatiotemporal nature of the WSS disturbances, however, without differentiation between physiological laminar oscillations and turbulence-related WSS (tWSS) fluctuations. Also, much attention has been focused on magnetic resonance (MR) WSS estimations, so far with limited success; promoting the need of a near-wall surrogate marker. In this study, a new approach is explored to characterize the tWSS, by taking advantage of the tensor characteristics of the fluctuating WSS correlations, providing both a magnitude and an anisotropy measure of the disturbances. These parameters were studied in two patient-specific coarctation models (sever and mild), using large eddy simulations, and correlated against near-wall reciprocal Reynolds stress parameters. Collectively, results showed distinct regions of differing tWSS characteristics, features which were sensitive to changes in flow conditions. Generally, the post-stenotic tWSS was governed by near axisymmetric fluctuations, findings that where not consistent with conventional WSS disturbance predictors. At the 2–3 mm wall-offset range, a strong linear correlation was found between tWSS magnitude and near-wall turbulence kinetic energy (TKE), in contrast to the anisotropy indices, suggesting that MR-measured TKE can be used to assess elevated tWSS regions while tWSS anisotropy estimates request well-resolved simulation methods.

1. Introduction

The random nature of transitional and/or turbulent-like hemodynamics is known to increase the flow perfusion pressure and occasionally even cause blood damage, while its phenotypic interaction with the endothelium and underlying arterial structure is less understood (Baratchi et al., 2017; Barbee, 2002; Chistiakov et al., 2017). *In-vivo*, these flow regimes are manifested by a wide spectrum of irregular velocity and pressure fluctuations (e.g. from shear-layer destabilization and vortical breakup), with much higher frequency components compared to laminar flow pulsations (Lee et al., 2008; McCormick et al., 2012), promoting a very unfavorable multidirectional wall shear stress (WSS) environment accompanied with strong spatiotemporal gradients.

Under physiologic laminar flow conditions, unidirectional-dominant WSS plays an important role in maintaining vascular integrity and functionality, via flow-sensitive endothelial cells (ECs), by regulating e.g. hemostasis, vascular tone and permeability as well as promote protective stimulus against atherosclerosis, thrombosis and wall remodeling (Davies, 2009). Conversely, pathologic disturbed flows, characterized by more spatiotemporal varying WSS, have been linked to endothelial dysfunction (impairing critical mechanostranduction pathways) and increased susceptibility and progression of several vascular diseases (Chiu and Chien, 2011; Cunnane et al., 2017; Kwak et al., 2014).

The first phenotypic indication of turbulent hemodynamics was reported half a century ago in animal models (Flaherty et al., 1972; Fry, 1968), observing ECs disorientations, which later were coupled to the unsteady nature of the WSS (Davies et al., 1986). Since then, several *in-vitro* studies have associated turbulence with elevated ECs activity and misalignment in regions of high WSS gradients (DePaola et al., 1999, 1992), impairment of vasoactive elements

* Corresponding author at: Department of Management and Engineering, Linköping University, SE-581 83 Linköping, Sweden.
E-mail address: magnus.andersson@liu.se (M. Andersson).

https://doi.org/10.1016/j.jbiomech.2019.01.016
0021-9290/

(Noris et al., 1995), different degree of cell elongation (McCormick et al., 2012), and promotion of inflammatory cells (Aoki et al., 2016). *In-vivo*, turbulent-like flow is typically manifested in regions of unfavorable anatomical obstructions (e.g. stenoses, valvular disease, bifurcations, aneurysms and sharp bends), lesions or intervention-related sites (e.g. grafts and mechanical heart valves) (Davies, 2009), which can be further amplified during exercise (Arzani et al., 2014; Lee et al., 2008). However, current advancement in magnetic resonance imaging (MRI) and computational techniques suggests even more frequent occurrences in the cardiovascular system (Bozzetto et al., 2016; Ha et al., 2018; Valen-Sendstad et al., 2013, 2014; Zajac et al., 2015). Recently, turbulent hemodynamics were coupled to specific upregulated endothelial signaling pathways associated to plaque formation (Wang et al., 2016), activities which were not present in the laminar flow cases, thus suggesting a possible targeting treatment against atherosclerosis.

Accurate MRI-assessment of the WSS magnitude is, to date, insufficient *in-vivo* due to near-wall limitations (Petersson et al., 2012; Piatti et al., 2017), so far only being comparable with state-of-the-art computational fluid dynamics (CFD) on a trend basis (Potters et al., 2014, 2015). Attempts to find methods to estimate the turbulence-related WSS (tWSS) in 4D Flow CMR (four-dimensional cardiovascular magnetic resonance) have been made in the immediately proximity of the wall (Ziegler et al., 2017), suggesting the near-wall voxel resolution to be insufficient and the need of a proxy parameter. Recently, 4D Flow CMR schemes have been developed to assess the complete Reynolds stress tensor in turbulent flows (Haraldsson et al., 2015; Kefayati et al., 2015), so far indicating promising results against CFD (Ha et al., 2016, 2017), hence providing access to near-wall parameters that potentially could be correlated to the tWSS.

From high-resolution CFD, the tWSS magnitude can be estimated, and is traditionally done by considering the statistical cycle-to-cycle variance of the WSS signal (Gårdhagen et al., 2010; Lantz et al., 2012), which contrasts to other popular parameters such as oscillatory shear index (Ku et al., 1985) or transverse WSS (Peiffer et al., 2013) that approximates the overall, including physiological laminar WSS variations using time-averaging assumptions. In the fluid, the turbulence characteristics can be described by scalar invariants of the Reynolds stress tensor (Banerjee et al., 2007; Choi and Lumley, 2001), where e.g. the overall magnitude of the turbulence transport can be assessed by the turbulence kinetic energy (TKE, analog to the first invariant: I). From the Reynolds stress anisotropy tensor it is also possible to characterize the degree of turbulence anisotropy (second invariant: II) and nature of turbulence (third invariant: III). It is well known that turbulence anisotropy is enhanced due to the presence of the wall, enforcing the turbulent stresses to wall-align. However, even in wall-bounded flow, these mechanisms are complex, where the wall-distance and nature of the flow have been shown to play an important role in regulating the level of anisotropy (Liu and Pletcher, 2008; Manna et al., 2012, 2015).

Near-wall TKE has indicated a positive relationship with tWSS magnitude under steady peak flow conditions using MR-realistic data aggregation (Ziegler et al., 2017). In pulsatile flows, however, *in-vivo* comparable large-amplitude oscillations have shown to have major impact on near-wall turbulence behavior (Manna et al., 2012, 2015). As such, the physiological relevance of steady flow regimes may be questionable. In pulsatile flows, our earlier work (Andersson et al., 2017) suggested a potential correlation between tWSS magnitude and TKE, however, not in a MRI-feasible wall-offset range.

In this study, we first propose a new, more complete approach to characterize WSS disturbance in turbulent-like flow, by considering the invariant properties of a second-moment correlation tensor on the WSS fluctuations (analog to the Reynolds stress tensor), which can estimate both the magnitude and degree of anisotropy of the turbulence-related WSS. These parameters were examined under patient-specific flow pulsatile conditions using large eddy simulations (LES) on an aortic coarctation (CoA) model before (pre-op) and after intervention (follow-up); representing two relevant examples of pathological flows with different turbulent strength. In addition, we also investigated the relation between these tWSS parameters and their near-wall reciprocal parameters from the Reynolds stress tensor, both qualitatively and using correlations (monotonic and linear), with the aim to find a wall-offset limit (or range) at which these parameters commute.

2. Methods

In this section, only a brief description of the method is given. More details can be found in previous studies (Andersson et al., 2015, 2017) and Supplementary materials.

2.1. MRI acquisition and segmentation

Patient-specific data were acquired using a 1.5 T Philips Achieva MRI scanner and reconstructed using Segment (Heiberg et al., 2010) to obtain geometries (Fig. 1) and supracoronary flow conditions. Proper consents from the patient and local ethics committee were acquired.

2.2. Computational model and simulation methods

Measured systolic flow rate was assigned to the ascending aorta (AAo) inlet, whilst the outflow trough the arch branches were governed by a square law. The inlet descending aorta (DAo) Reynolds number (Re) was in both cases similar in temporal-mean ($Re \approx 950$) and peak values ($Re \approx 3500$). The no-slip wall was assumed to be rigid. The fluid viscosity followed the Carreau blood model, where non-Newtonian rheology have shown to delay turbulence-transition and reduce turbulence levels (Andersson et al., 2015, 2017; Khan et al., 2018). LES, along with the WALE subgrid model (Nicoud and Ducros, 1999), was used to resolved the energy-containing turbulent scales. Simulations were performed in ANSYS CFX 15.0 (ANSYS Inc, Canonsburg, PA, USA). Sensitivity analysis showed that 3 million hexahedral cells, keeping the Courant-Friedrichs-Lewy condition below 5 and using 80 cardiac cycles gave satisfactory phase-averaged results.

2.3. Hemodynamic parameters

In this section, an overview of the investigated parameters and their definitions are presented (Table 1). Reynolds decomposition (Pope, 2001) was utilized to form the six independent phase-averaged components of the correlation tensors. This tensor was normalized by its trace and divided into an isotropic (only diagonal elements) and anisotropic (traceless) part. The anisotropy tensor entails some unique characteristics, where e.g. the invariants (second: II, and third: III), or correlated eigenvalues, together describe different stress states of the turbulence (Lumley and Newman, 1977), which are bounded by triangular-like region known as the anisotropy invariant map (AIM) or Lumley triangle (Fig. 2). In fact, concerning the Reynolds stresses, any point can be realized in the AIM, while the invariant-relation for the WSS correlation tensor inherently is constrained to the two-component limit. Along this line, the tWSS can take two extreme states, i.e. WSS fluctuations that are (i) random and lacks any preferential directionality (two-component axisymmetric, 2C) or (ii) purely unidirectional (one-component, 1C). In the present study, we take advantage of these properties, using the first invariant of the isotropic tensor and second invariant of the anisotropy tensor to estimate the mag-

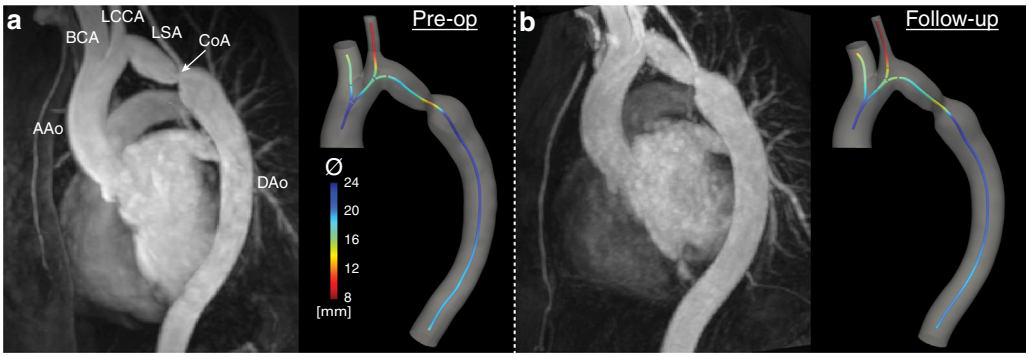

Fig. 1. Maximum intensity projection (MIP) MR angiogram and computational domain. a and b, MIP (left) and segmented intraluminal boundary of the computational domain (right) with imposed centerlines displaying the local diameter variations. a, before intervention (pre-op), with abbreviated arterial sites: ascending aorta (AAo), brachiocephalic artery (BCA), left common carotid artery (LCCA), left subclavian artery (LSA), coarctation of the aorta (CoA, white arrow) and descending aorta (DAo). b, after intervention (follow-up). Note that the LSA was not included in the computational models.

Table 1
Definition of hemodynamic parameters. The phase-averaging was performed over N = number of cardiac cycles (between the 6th to 85th cycle). Symbols are: Φ_i = generic vector variable, φ = generic scalar variable, T = constant cardiac period, T_φ = time-averaging period, t = time in cardiac cycle, Φ_i'' = phase-averaged fluctuations, ρ = fluid density (1060 kg/m^3), u_i = velocity components, τ_i = wall shear stress components, and δ_{ij} = Kronecker delta.

Operators and parameters	Definition	Notation
Phase-averaged operator	$\langle\Phi_i\rangle(\mathbf{x},t)=\frac{1}{N}\sum_{n=0}^{N-1}\Phi_i(\mathbf{x},t+nT)$	$\mathbf{x}(x,y,z)$
Time-averaged operator	$\overline{\langle\varphi\rangle}(\mathbf{x})=\frac{1}{T_\varphi}\int_{t_0}^{t_0+T_\varphi}\langle\varphi\rangle(\mathbf{x},t)\mathrm{d}t$	
Reynolds decomposition	$\Phi_i''(\mathbf{x},t)=\Phi_i(\mathbf{x},t)-\langle\Phi_i\rangle(\mathbf{x},t)$	
Correlation tensor	$\langle\boldsymbol{C}_{ij}\rangle=\begin{bmatrix}C_{11} & C_{12} & C_{13}\\ \vdots & C_{22} & C_{23}\\ \vdots & \cdots & C_{33}\end{bmatrix}=\langle\Phi_i''\Phi_j''\rangle=\frac{1}{N}\sum_{n=0}^{N-1}\Phi_i''\Phi_j''$	3×3 sym.
Correlation tensor decomposition	$\langle\boldsymbol{C}_{ij}\rangle=\langle\boldsymbol{C}_{kk}\rangle(\delta_{ij}/3+\langle\boldsymbol{a}_{ij}\rangle)$	$\boldsymbol{a}_{kk}=0$
Reynolds stress parameters	$\langle\mathbf{R}_{ij}\rangle=\langle u_i''u_j''\rangle,\langle\boldsymbol{b}_{ij}\rangle=\langle\boldsymbol{R}_{ij}\rangle/\langle\boldsymbol{R}_{kk}\rangle-\delta_{ij}/3$	$\Phi_i=u_i$
Turbulent kinetic energy	$\mathrm{TKE}=\frac{1}{2}\rho\overline{\langle\boldsymbol{R}_{kk}\rangle}$	
2nd invariant of the anisotropy tensor	$\mathrm{II}=\overline{\langle\boldsymbol{b}_{ij}\rangle\langle\boldsymbol{b}_{ji}\rangle}$	$\in[0,\ \frac{2}{3}]$
3rd invariant of the anisotropy tensor	$\mathrm{III}=\overline{\langle\boldsymbol{b}_{ij}\rangle\langle\boldsymbol{b}_{jk}\rangle\langle\boldsymbol{b}_{ki}\rangle}$	$\in[-\frac{1}{36},\frac{2}{9}]$
Anisotropy index (Reynolds stresses)	$\mathrm{AI_b}=\frac{3}{2}\mathrm{II}$	$\in[0,\ 1]$
Wall shear stress parameters	$\langle\mathbf{T}_{ij}\rangle=\langle\tau_i''\tau_j''\rangle,\langle\boldsymbol{w}_{ij}\rangle=\langle\mathbf{T}_{ij}\rangle/\langle\mathbf{T}_{kk}\rangle-\delta_{ij}/3$	$\Phi_i=\tau_i$
Turbulent-related WSS magnitude	$\mathrm{tWSS}=\overline{\sqrt{\langle\mathbf{T}_{kk}\rangle}}$	
Anisotropy index (tWSS)	$\mathrm{AI_w}=2\left(\overline{\langle\boldsymbol{w}_{ij}\rangle\langle\boldsymbol{w}_{ji}\rangle}\right)-\frac{1}{3}$	$\in[0,\ 1]$
Non-redistributed $\mathrm{AI_w}$	$\widetilde{\mathrm{AI}}_\mathrm{w}=\frac{3}{2}\overline{\langle\boldsymbol{w}_{ij}\rangle\langle\boldsymbol{w}_{ji}\rangle}$	$\in[\frac{1}{4},\ 1]$

nitude and degree of one-componentality of tWSS, respectively. The latter parameter, referred to as the anisotropy index of the tWSS (denoted: $\mathrm{AI_w}$), was normalized and redistributed between 0 and 1 along the two-component limit, hence $\mathrm{AI_w}=0$ correspond to an isotropic state while $\mathrm{AI_w}$ near unity signifies unidirectional tWSS fluctuations. In analog fashion, corresponding parameters were also defined for the Reynolds stress tensor, to characterize the near-wall turbulence. Here, the TKE and normalized II (denoted: $\mathrm{AI_b}$) was used to represent the magnitude and level of anisotropy of the turbulence, respectively. An alternative approach could be to also use a linear representation of anisotropy invariants, providing linear weights ([0, 1]) of each limiting states (Banerjee et al., 2007), which would be practical to directly assess the level of anisotropy.

2.4. Data and correlation assessments

The relation between the wall and near-wall parameters were evaluated both qualitatively (maps) and by monotonic (Spearman's ρ) and linear (Pearson's r) correlations. The correlation strength, assuming only positive correlations, was differentiated into three intervals: strong ($0.9\leq r$), modest ($0.7\leq r<0.9$) and weak ($r<0.7$).

3. Results

3.1. Flow characteristics

At volumetric peak of turbulence, the velocity magnitude showed a distinct eccentric post-stenotic jet pre-op (Fig. 3a), accompanied with elevated TKE regions (Fig. 3b), with an evident impact on the tWSS magnitude along the outer-curved wall (Fig. 3c). Here, the follow-up case had more vessel-centered turbulent flow, resulting in substantially lower tWSS intensities. Throughout the pre-op cardiac cycle (length = 1 s, systole = 0.05–0.5 s), four different flow stages (S1–S4) were identified in the post-stenotic region:

S1. mid-to-late acceleration [0.1, 0.15): eccentric jet formation, shear-layer roll (vortex ring), with evident posterior wall interaction.

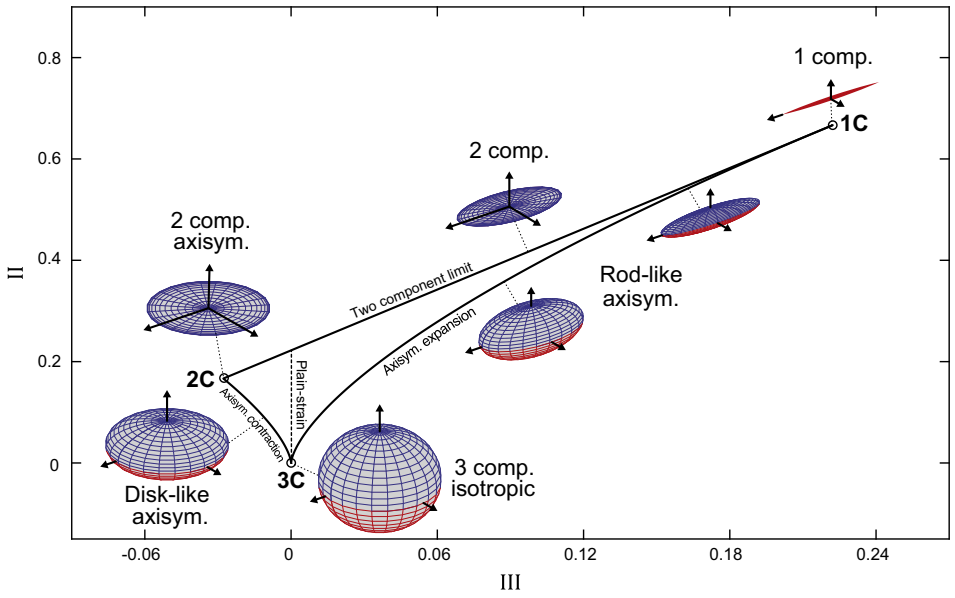

Fig. 2. Anisotropic invariant map (AIM) of the turbulent stress field in invariant coordinates. All physically realizable states of turbulence can be constrained to a triangular-like region, derived from the invariant properties (second and third invariant: II and III) of the anisotropic Reynolds stress tensor, describing the relative size of the principal normal stresses (see glyphs examples). The AIM is limited to three primary stress shapes: one-component (1C), two-component axisymmetric (2C) and three-component isotropic (3C) turbulence. These states are joint by different boundaries: axisymmetric expansion (rod-like turbulence), axisymmetric contraction (disk-like turbulence) and the two-component limit (pancake-like turbulence). Another, special state, is the plain-strain limit (III = 0), where the turbulence only commute in planes.

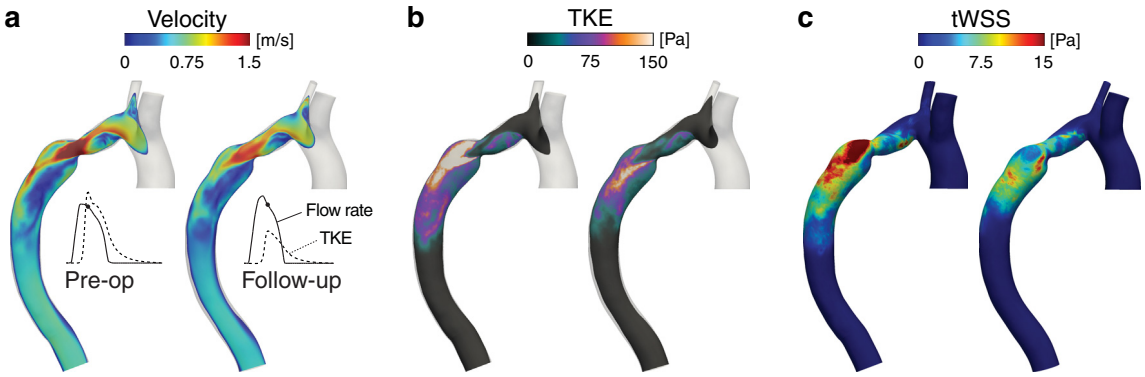

Fig. 3. Instant flow characteristics at volumetric peak of turbulence. a–c, phase-averaged hemodynamic parameters assessed before (pre-op) and after intervention (follow-up), left and right vessel respectively. Each snapshot was taken when the volumetric amount turbulent kinetic energy (TKE) (insets, dashed line) maximized, which occurred at early flow deceleration (insets, solid line and marker). a, centerplane velocity magnitude. b, centerplane TKE. c, magnitude of the turbulence-related wall shear stress (tWSS).

S2. peak-to-early deceleration [0.15, 0.2): formation and partly breakdown of coherent, streamwise-traveling vortical structures, with initial evidence of localized turbulent spots.
S3. early-to-mid deceleration [0.2, 0.4): initial jet shear-layer destabilization and vortical breakup, followed by major turbulence intensification in the proximal region, towards the posterior wall (Fig. 4a). Also denoted: early-flow-deceleration (EFD).
S4. mid-to-late deceleration [0.4, 0.6): jet collapse and gradual flow relaminarization, with near isotropic core turbulence (Fig. 4c). Also denoted: late-flow-deceleration (LFD).

Across S1–S3, the flow displayed clear helical characteristics, features which are well known to exist in aortic flows (Morbiducci et al., 2011). At the tip of the aortic arc kink, distinct flow separation occurred, with shear-layer shedding and vortical formation/breakdown (S1–S2), followed by turbulence intensification and increased anisotropy (Fig. 4a and c). At follow-up, the post-stenotic turbulence was governed by two joining shear-layers, rather than a distinct jet, here resulting in reduced TKE levels but enhanced near-wall anisotropy (Fig. 4b). The critical Reynolds number for turbulence onset occurred at and just prior to peak flow for the pre-op ($Re_{crit} \approx 2890$) and follow-up ($Re_{crit} \approx 2820$) case, respectively (see Supplementary materials).

3.2. Turbulence-related WSS before and after intervention

Comparing the tWSS magnitude at EFD (Fig. 5a and b), a much stronger and distinct turbulent spot could be seen pre-op, along the outer-curvature of the post-stenotic region, with more than two-fold higher intensities along the posterior side compared to follow-up (Fig. 4a and 5a, 0.5D). Here, the tWSS anisotropy was highest ($AI_w \approx 0.5$) in the upstream and CoA region, mostly in collocation with low tWSS, while being generally low ($AI_w < 0.1$) in the post-stenotic region. However, distinct areas of higher anisotropy ($AI_w \approx 0.2–0.8$) were noticed (Fig. 5a, A1–P2), some collocated with high tWSS magnitude (P2). In this cardiac phase, these features were either preserved (A2), strengthen (P1), dampened (P2) or entirely suppressed (A1) at follow-up. At LFD the tWSS magnitude were reduced substantially (Fig. 6a and b), with more diffused intensity patterns. Here, most of the elevated anisotropy

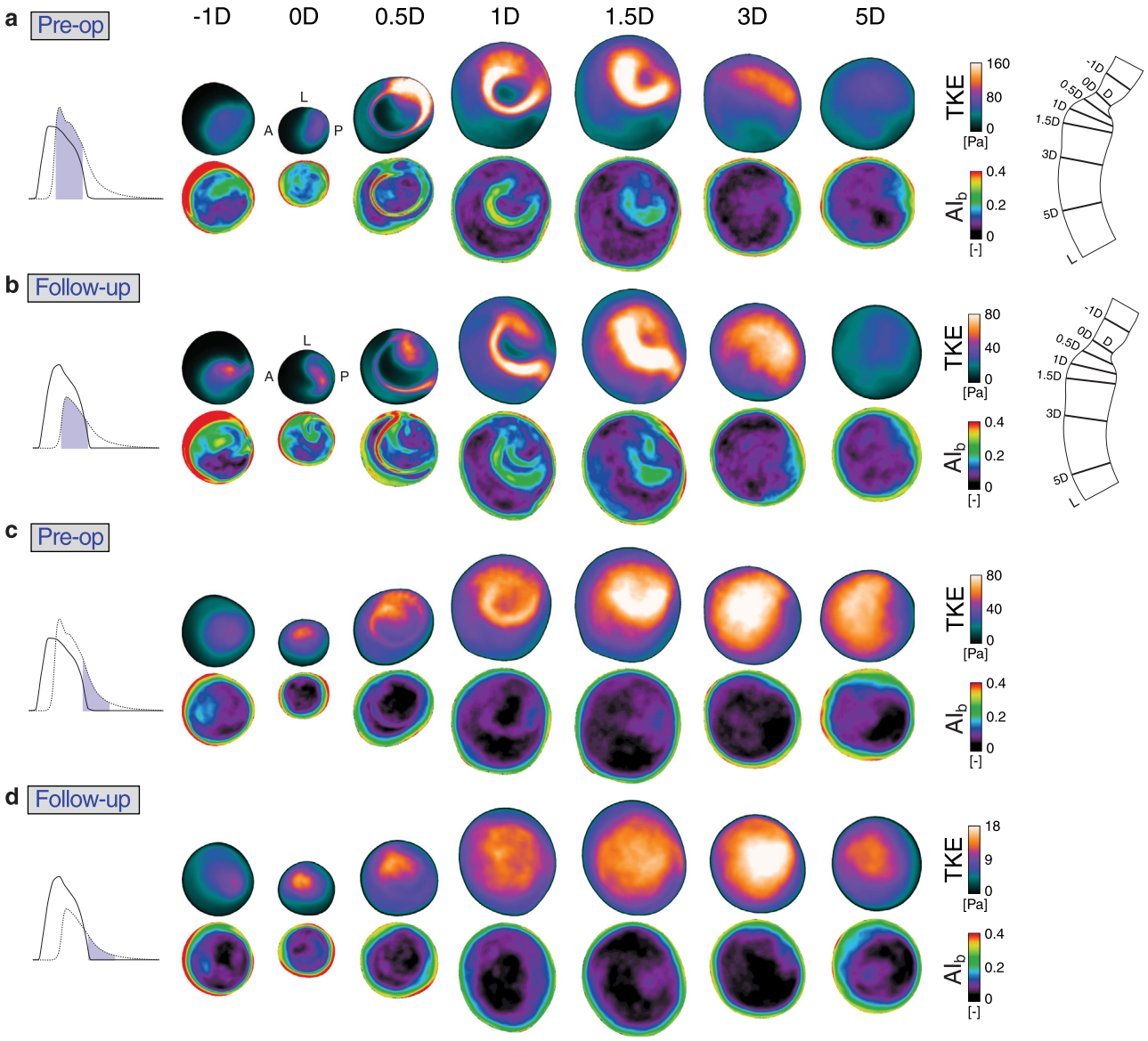

Fig. 4. Cross-sectional view of the turbulent flow characteristics. a–d, in-plane slices assessed at seven different location along the descending aorta (DAo) centerline, before (pre-op) and after intervention (follow-up), based on mean diameter (D) offsets at the aortic coarctation (0D). The top of each slice (denoted: L) follows the outer curvature of the DAo (Fig. 5, dashed line). For reference, the anterior (A) and posterior (P) sides were also included. Colormaps were adjusted to show the slices combined 99th percentile parameter range. For parameter definitions see Table 1. a and b, early flow deceleration. c and d, late flow deceleration. (For interpretation of the references to color in this figure legend, the reader is referred to the web version of this article.)

features were shifted towards the anterior side, with some preserved (pre-op: A1) or near suppressed (A2 and P1, pre-op: P2) locations.

The AI_w area ratio distribution (Fig. 7), showed that most of the tWSS anisotropy are realized just prior to the plain-strain limit ($AI_w \approx 0.33$, $AI_w \approx 0.11$) in both cases. At EFD, areas of higher anisotropy ($AI_w > 0.6$, $AI_w > 0.47$) could be seen, which were not present at LFD. In fact, for the follow-up case, matching or even larger areas of high anisotropy could be seen in comparison to pre-op.

3.3. Relation against near-wall parameters

Taken collectively, a close resemblance was seen between the tWSS magnitude and most wall-proximal TKE maps (Fig. 5a, b and 6a, b), which appeared to diminish beyond the 2 mm wall-offset mark. Comparing the anisotropy indices, only a good agreement was seen for the innermost 0.1 mm wall-offset region, whereafter certain features started to weaken (e.g. A1, P1 and P2). Overall, the radial thickness of the "anisotropy layer" was around 1 mm in the post-stenotic region, with a tendency to thicken further downstream (also see Fig. 4), while more isotropic characteristics were seen beyond this wall-distance.

In the scattergrams, an apparent linear relation was seen between the tWSS magnitude and TKE at both cardiac phases (Fig. 5c and 6c), which was only evident at 0.1 mm wall-offset for the anisotropy indices. The correlations indicated an overall strong ($0.9 \leq \rho$) monotonic dependency between tWSS magnitude and TKE over the entire wall-offset range (Fig. 5d and 6d). The Pearson correlation suggested a strong linear-dependency ($0.9 \leq r$) up to around 2–3 mm from the wall, whereafter the relation only was moderate at EFD. The Spearman relation between AI_w and AI_b showed faster decorrelation versus wall distance, being weak ($\rho < 0.7$) before the 0.5 mm wall-offset mark. For these indices, a slight improved linear correlation was observed, but with similar overall decaying tendencies.

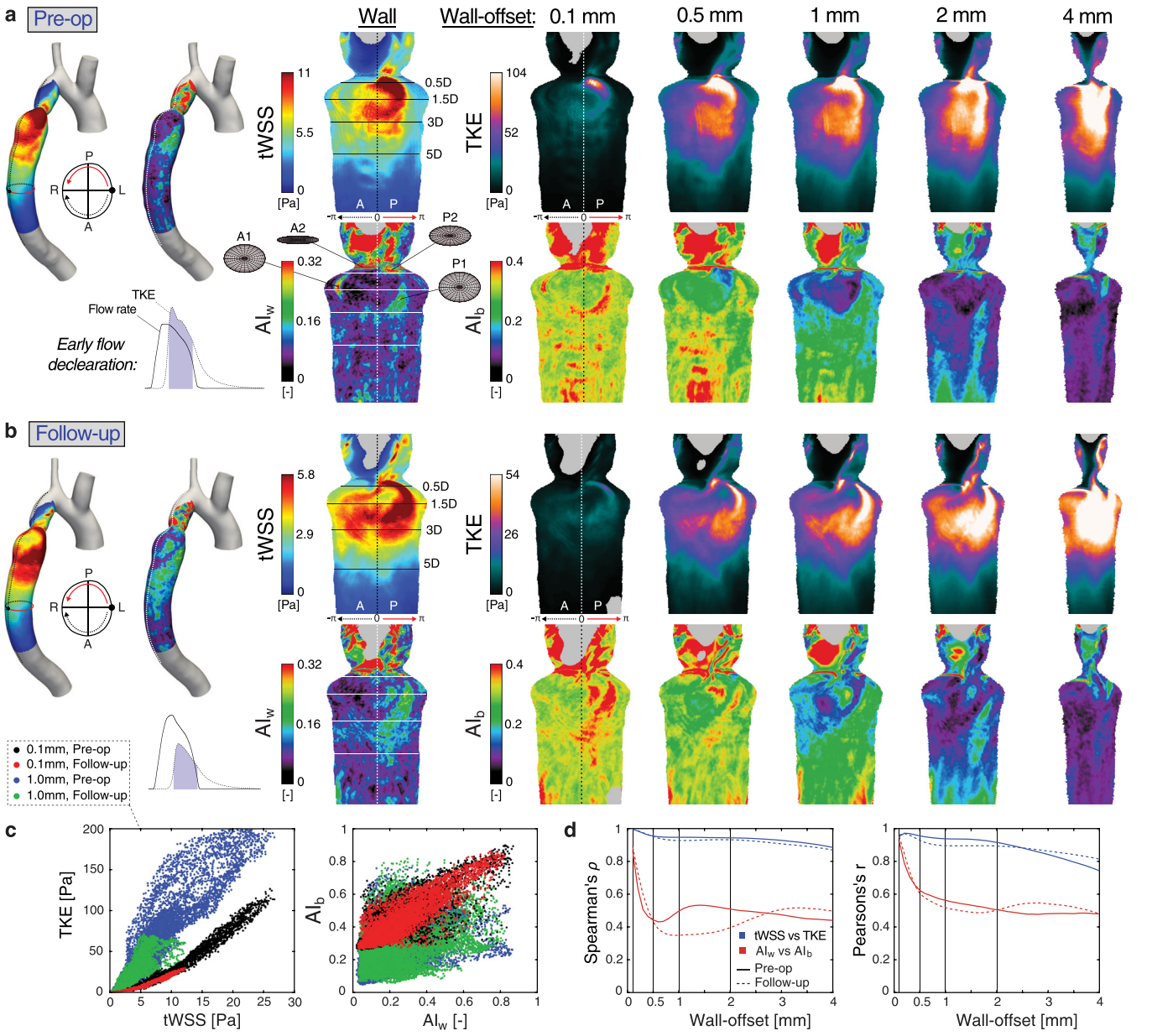

Fig. 5. Relation between the wall and near-wall turbulence parameters at early flow deceleration. a and b, descending aorta (DAo) maps of WSS-related parameters (tWSS and AI_w) and near-wall parameters (TKE and AI_b) at different wall-offsets (0.1, 0.5, 1, 2 and 4 mm). For parameter definition see Table 1. The circumferential reference point follows the outer curvature of the vessel (dashed line, reference point L) and unfolds the data along the anterior (A) and posterior (P) side. For visualization purposes, map aspect ratios are asymmetrical and colormaps adjusted to show their 95th percentile range. Left margin, vessel perspective of the WSS-related parameters and time-averaging in the cardiac phase (insets, shaded area). The lowest magnitude values (below 2nd percentile range) were excluded in all maps. For reference, some cross-sectional slice-positions (horizontal lines) were added (see Fig. 4). a, maps before intervention (pre-op). A1–P2: post-stenotic feature locations, with AI_w glyphs showing the relative magnitude of the WSS fluctuations in the two principal directions. b, maps after intervention (follow-up). c, scattergrams at 0.1 and 1 mm wall-offsets. d, Spearman's rank correlation (ρ) and Pearson's correlation coefficient (r) at different wall-offsets (0.1–4 mm). Vertical lines mark the map locations (a and b). All correlation where significant ($p < 0.001$). (For interpretation of the references to color in this figure legend, the reader is referred to the web version of this article.)

The surface area distribution of the anisotropy indices showed a clear alignment at 0.1 mm wall-offset (Fig. 7). Generally, at greater wall-offsets a shift towards more isotropic characteristics could be noticed for AI_b. However, at EFD and 0.5 mm wall-offset (Fig. 7a), the distribution of higher values ($AI_b > 0.35$) agreed well with AI_w distribution, while being underestimated at LFD (Fig. 7b).

4. Discussion

In this study, we explored a new approach to characterize the tWSS in patient-specific flows, by taking advantage of the tensor characteristics of the fluctuating WSS correlations, providing both a magnitude and an anisotropy measure of the local disturbances. Taken collectively, results showed a clear tWSS magnitude reduction after intervention due to less energetic and vessel-centered turbulence, while the degree of anisotropy generally was low in the post-stenotic region for both cases. However, pre-op sizable regions of higher anisotropy were found near the turbulence spot, characteristics that changed after follow-up. Near-wall correlations showed an overall strong linear relation between tWSS magnitude and TKE up to 2–3 mm wall-offset distance (Fig. 5d, and 6d), while the relation between the anisotropy indices was only significant in the innermost wall-region.

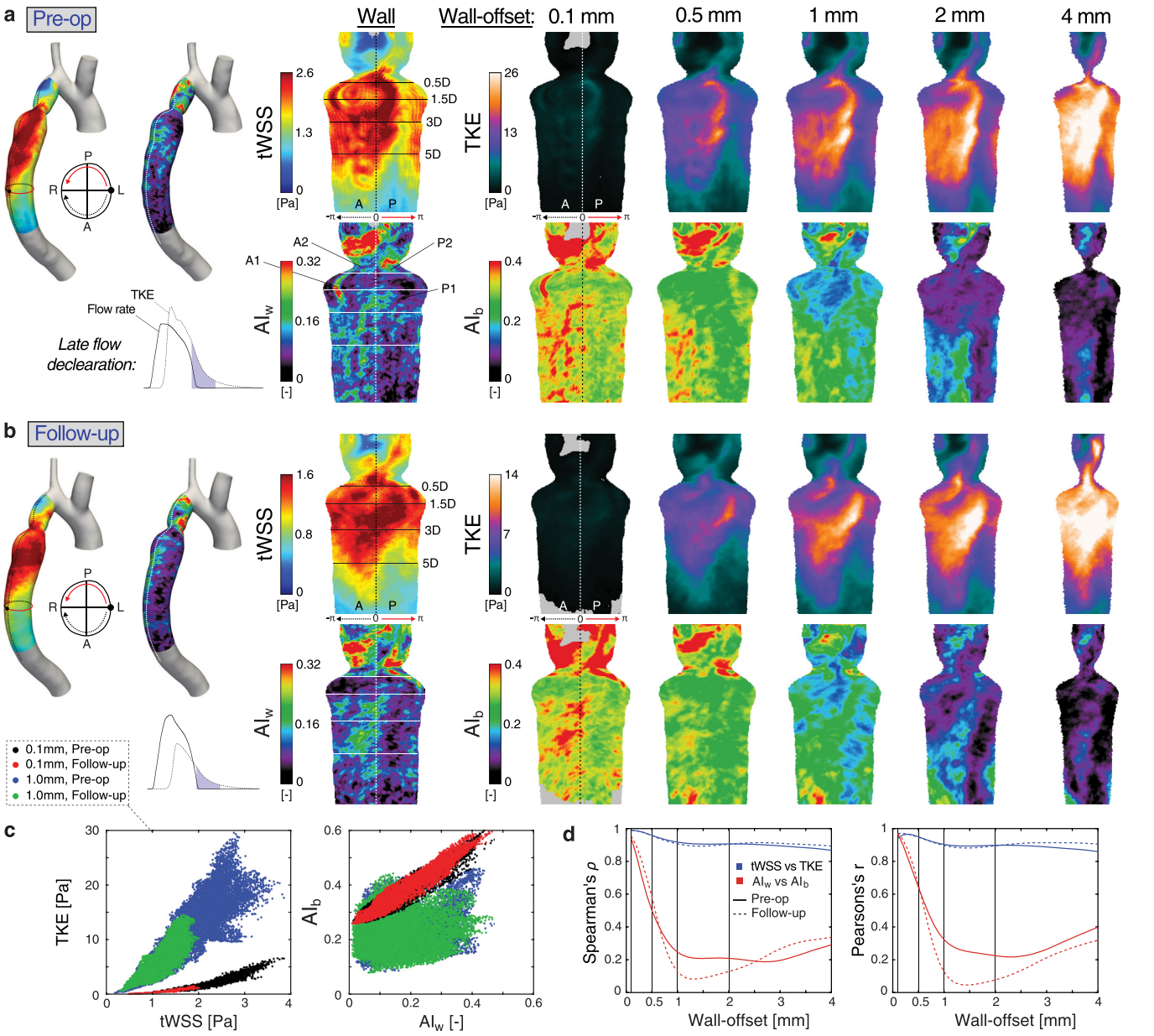

Fig. 6. Relation between the wall and near-wall turbulence parameters at late flow deceleration. a and b, for abbreviations and more detail see Fig. 5. a, maps before intervention (pre-op). b, maps after intervention (follow-up). c, scattergrams at 0.1 and 1 mm wall-offsets. d, Spearman's rank correlation (ρ) and Pearson's correlation coefficient (r) at different wall-offsets (0.1–4 mm). Vertical lines mark the map locations (a and b). All correlation where significant ($p < 0.001$).

Turbulent-like flows is today more frequently detected at different cardiovascular sites, thanks to more sophisticated techniques such as 4D Flow CMR and CFD, and is believed to be an important contributor to ECs dysfunction and atherogenesis (Baratchi et al., 2017; Davies, 2009; Gimbrone and García-Cardeña, 2016; Wang et al., 2016), owing to the unstable WSS environment caused by flow instabilities in the near-wall region. Over the years, a wealth of parameters has been suggested to characterize the spatiotemporal nature of the WSS vector in hemodynamics, from more traditional such as TAWSS (time-averaged WSS) and OSI (oscillatory shear index), to more recent, directional- or gradient-based descriptors (Arzani and Shadden, 2016; Morbiducci et al., 2015; Peiffer et al., 2013). These parameters cannot make distinction between unsteady, but physiological laminar flow oscillations, and cycle-to-cycle variabilities associated to turbulent-like flows. In pulsatile flows, the turbulence-related WSS is typically estimate from the magnitude of the phase-averaged WSS fluctuations alone, either as vector components in idealized vessels (Gårdhagen et al., 2010) or by the L_2 norm in patient-specific geometries (Andersson et al., 2017; Lantz et al., 2012); in common lacking insights into the characteristics of the tWSS. Inspired by the anisotropy invariant theory, typically used to characterize turbulence Reynolds stresses, we defined a new parameter that describes the different tWSS states across the two-component limit. This parameter can differentiate between vascular regions that overtime are exposed to e.g. unidirectional-dominant or entirely random tWSS fluctuations. Attaining a more complete picture of tWSS properties, including both strength and degree of anisotropy of the fluctuations, may enable better characterization of undesirable near-wall flow features and complement other WSS descriptors; towards identifying disease-prone regions.

In this study, results showed a clear difference in flow behavior between the both cases (Figs. 3 and 4), despite comparable Reynolds numbers. Pre-op, much stronger turbulence activities were

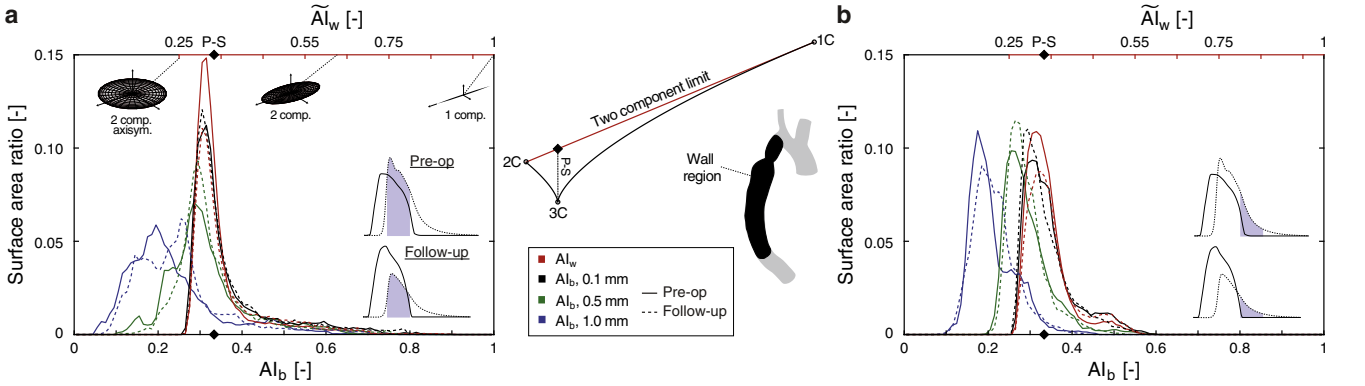

Fig. 7. Surface area distribution between the wall and near-wall anisotropy indices. a, b, ratio between the surface area entailed by local intensity intervals (discretized into 100 bins) and the total surface area (inset, wall region) before (pre-op) and after intervention (follow-up). Note, for easier comparison, the non-redistributed anisotropy index AI_w was used (see Table 1), which conforms directly with the two-component limit of the Lumley triangle (inset, middle), also see Fig. 2. The Reynolds stress anisotropy index (AI_b) were assessed at three different wall-offset distances (0.1, 0.5 and 1 mm). For reference, a marker for the plain-strain (P-S) position was added. a, early flow deceleration. b, late flow deceleration.

noted along the post-stenotic outer-curved wall, as a result of a more distinct, stronger and eccentric jet flow. The observed secondary flow features (streamwise vortex ring, shear-layer destabilization) and timing of turbulence-transition/intensification, seen in this study, have been confirmed experimentally (Ahmed and Giddens, 1984; Khalifa and Giddens, 1981) and numerically (Varghese et al., 2007) in idealized pulsatile stenotic flows, as well as in *in-vivo* CoA TKE measurements (Arzani et al., 2012; Lantz et al., 2013).

Along the outer-curvature of the post-stenotic region, a clear spot of elevated tWSS magnitude was depicted at the first distal CoA diameters in both cases (Figs. 5 and 6), with considerably higher intensities pre-op. Here, a majority of the post-stenotic tWSS were governed by nearly axisymmetric fluctuations (Figs. 5–7), evident by the generally low AI_w, while in large parts of the upstream region tWSS appeared to be more anisotropic. These findings are not consistent with the general view of turbulent flow subjected to axisymmetric contraction (positive axial strain) or expansion (negative axial strain) (Banerjee et al., 2008), where the near-wall Reynolds stresses is expected to approach the 2C and 1C limiting states (Fig. 2), respectively. It should be noted, however, that a large part of the upstream flow were governed by transitional type of flow, characteristics which generally are hard to capture completely, even with LES, where higher-order CFD methods may be warranted. In the post-stenotic region, sizeable spots of elevated anisotropy were detected (Figs. 5 and 6, feature locations), which interestingly either was absent, attenuated or amplified at follow-up and/or between the early and late flow deceleration phase; collectively highlighting the AI_w parameter sensitivity to change in flow characteristics. Compared to our previous study (Andersson et al., 2017), the location of these features did not appear to have a consistent relation against the transverse WSS nor OSI. Here, high OSI values, as in the fixed-point regions of the time-averaged WSS vector field, could be connected to regions of low degree of tWSS anisotropy, but not vice versa. Likewise, transverse WSS generally predicted major multidirectional WSS disturbances along the posterior side, unlike the AI_w parameter that suggested these properties in a majority of the post-stenotic turbulent region. One reason for the latter differences could be associated to the fact that the AI_w only considers the relative strength of the fluctuating components, and hence cannot relate to the anisotropy magnitude. An improved description may be attained by including additional anisotropy tensor attributes, such as the Frobenius norm. Another explanation for these dissimilarities could be that these common descriptors essentially are dominated by low-frequency laminar-related content, in contrast to the tWSS-parameters. In a recent study (Khan et al., 2017), Fourier decomposition was proposed on the WSS signal, to only assess the pathological high-frequency range and its energy content, where the so called spectral power index was used to differentiate between region of high and/or low level of flow instabilities. Regarding WSS, this parameter is analog to tWSS magnitude, but, unlike AI_w, cannot take into account the anisotropic characteristics of these instabilities. Although, a possible advantage with this filtering approach is the option to control the spectral-content in any given parameter, e.g. to remove intermediate frequencies that are more associated to cycle-to-cycle variance of coherent secondary flow features. As such, it would be possible to distinguish in which frequency band the tWSS parameters are most active.

To enable MRI-predictions of tWSS-prone cardiovascular region may be valuable to better correlate areas of endothelial and biological dysfunctionality, improving risk assessment and treatment strategies. In this study we therefore investigate the potential to find a near-wall surrogate tWSS marker, which potentially could be measured by the recent developed 4D Flow CMR techniques (Haraldsson et al., 2015; Kefayati et al., 2015). Here, the natural choice was to explore these correlations against the corresponding properties of the Reynolds stress tensor, with the hypothesis that near-wall TKE and AI_b will, at some unknown wall-offset distance, strongly-commute with the tWSS magnitude and AI_w, respectively. In summary, results showed an overall strong monotonic and linear relation between tWSS magnitude and TKE up to 2–3 mm wall-offset distance, while the anisotropy indices (AI_w vs AI_b) only correlated well in the innermost wall-region (~0.1 mm), with no substantial difference between the flow cases or cardiac phases (Fig. 5d and 6d). Considering typical spatial resolution used in 4D Flow CMR, ~1.5–3 mm isotropic voxels (Dyverfeldt et al., 2015), these findings suggest that the tWSS magnitude can be estimated by near-wall TKE, without severe partial volume effects, while tWSS anisotropy estimations request well-resolved CFD methods.

The used CFD method contain assumptions and limitations, which are not believed to change the generality of the findings in this study, see previous work (Andersson et al., 2015) and discussion in the Supplementary materials. While this study focused on linear correlations, it should be notated that a strong monotonic relation could also be non-linear. The correlation assessment were paired according to their shortest Euclidean distance, while an alternative could be to account for different directions, include a wider spatial region (Lee et al., 2009; Ziegler et al., 2017) or considered other correlation methods (Rowland et al., 2015). In this study

we only assessed scalar quantities related to the magnitude and degree of anisotropy of the tWSS. Further investigations could be to compare these parameters against features of the WSS vector fields and near-wall flow structures (Arzani and Shadden, 2018; Chong et al., 2012), other tensor quantities (e.g. structural information and turbulence orientation) and include barycentric map visualization (Banerjee et al., 2008; Emory and Iaccarino, 2014). Only two patient-specific flows were investigated in this study, next could be to explore a larger number of different flow characteristics (e.g. different Reynolds/Womersley numbers and vascular regions), include spectral-content analysis and perform 4D Flow CMR validations.

To conclude, in the present study we have stressed on the relevance between disturbed turbulence-related WSS and vascular disease, and proposed a new approach to differentiate between the magnitude and different states of the tWSS fluctuations. These parameters were studied in two patient-specific turbulent flow models, one severe and one mild coarctation, using scale-resolving CFD. For these flow cases, the anisotropy index depicted distinct regions of different tWSS characteristics, features that were sensitive to changes in flow conditions. Overall, however, the post-stenotic tWSS were governed by near axisymmetric fluctuations, findings that were not aligned with traditional parameters used for predicting WSS disturbances. Attempts to accurately measure WSS-based descriptors using MRI have been elaborated in many studies without success, where the near-wall resolution is a limited factor. In this work, we found a strong linear relation between tWSS magnitude and near-wall TKE, as far as 2–3 mm from the vascular wall in both cases, findings which suggest that 4D Flow CMR turbulence measurements may be sufficient to predict region exposed to elevated tWSS. The tWSS anisotropy index, however, showed a very narrow correlation versus wall-offset distance, suggesting that this parameter only can be obtained by well-resolved CFD.

Acknowledgements

The simulations were performed on resources provided by the Swedish National Infrastructure for Computing (SNIC) at National Supercomputer Centre (NSC).

Author contributions

Conception and design of the study: MA and MK. Experiments and interpretation of results: MA and MK. Draft of the manuscript: MA. All authors edited and revised the manuscript. All authors read and approved the final manuscript.

Competing financial interests

None.

Appendix A. Supplementary material

Supplementary data to this article can be found online at https://doi.org/10.1016/j.jbiomech.2019.01.016.

References

Ahmed, S.A., Giddens, D.P., 1984. Pulsatile poststenotic flow studies with laser Doppler anemometry. J. Biomech. 17, 695–705.
Andersson, M., Lantz, J., Ebbers, T., Karlsson, M., 2015. Quantitative assessment of turbulence and flow eccentricity in an aortic coarctation: impact of virtual interventions. Cardiovasc. Eng. Technol. 6, 281–293.
Andersson, M., Lantz, J., Ebbers, T., Karlsson, M., 2017. Multidirectional WSS disturbances in stenotic turbulent flows: a pre-and post-intervention study in an aortic coarctation. J. Biomech. 51, 8–16.
Aoki, T., Yamamoto, K., Fukuda, M., Shimogonya, Y., Fukuda, S., Narumiya, S., 2016. Sustained expression of MCP-1 by low wall shear stress loading concomitant with turbulent flow on endothelial cells of intracranial aneurysm. Acta Neuropathol. Commun. 4, 48.
Arzani, A., Dyverfeldt, P., Ebbers, T., Shadden, S.C., 2012. In vivo validation of numerical prediction for turbulence intensity in an aortic coarctation. Ann. Biomed. Eng. 40, 860–870.
Arzani, A., Les, A.S., Dalman, R.L., Shadden, S.C., 2014. Effect of exercise on patient specific abdominal aortic aneurysm flow topology and mixing. Int. J. Numeric. Methods Biomed. Eng. 30, 280–295.
Arzani, A., Shadden, S.C., 2016. Characterizations and correlations of wall shear stress in aneurysmal flow. J. Biomech. Eng. 138, 014503.
Arzani, A., Shadden, S.C., 2018. Wall shear stress fixed points in cardiovascular fluid mechanics. J. Biomech. 73, 145–152.
Banerjee, S., Ertunc, O., Durst, F., 2008. Anisotropy properties of turbulence. WSEAS International Conference. Proceedings. Mathematics and Computers in Science and Engineering.
Banerjee, S., Krahl, R., Durst, F., Zenger, C., 2007. Presentation of anisotropy properties of turbulence, invariants versus eigenvalue approaches. J. Turbul., N32
Baratchi, S., Khoshmanesh, K., Woodman, O.L., Potocnik, S., Peter, K., McIntyre, P., 2017. Molecular sensors of blood flow in endothelial cells. Trends Mol. Med. 23, 850–868.
Barbee, K.A., 2002. Role of subcellular shear–stress distributions in endothelial cell mechanotransduction. Ann. Biomed. Eng. 30, 472–482.
Bozzetto, M., Ene-Iordache, B., Remuzzi, A., 2016. Transitional flow in the venous side of patient-specific arteriovenous fistulae for hemodialysis. Ann. Biomed. Eng. 44, 2388–2401.
Chistiakov, D.A., Orekhov, A.N., Bobryshev, Y.V., 2017. Effects of shear stress on endothelial cells: go with the flow. Acta Physiol. 219, 382–408.
Chiu, J.-J., Chien, S., 2011. Effects of disturbed flow on vascular endothelium: pathophysiological basis and clinical perspectives. Physiol. Rev. 91, 327–387.
Choi, K.-S., Lumley, J.L., 2001. The return to isotropy of homogeneous turbulence. J. Fluid Mech. 436, 59–84.
Chong, M., Monty, J., Chin, C., Marusic, I., 2012. The topology of skin friction and surface vorticity fields in wall-bounded flows. J. Turbul., N6
Cunnane, C.V., Cunnane, E.M., Walsh, M.T., 2017. A review of the hemodynamic factors believed to contribute to vascular access dysfunction. Cardiovasc. Eng. Technol., 1–15
Davies, P.F., 2009. Hemodynamic shear stress and the endothelium in cardiovascular pathophysiology. Nature clinical practice. Cardiovasc. Med. 6, 16.
Davies, P.F., Remuzzi, A., Gordon, E.J., Dewey, C.F., Gimbrone, M.A., 1986. Turbulent fluid shear stress induces vascular endothelial cell turnover in vitro. Proc. Natl. Acad. Sci. 83, 2114–2117.
DePaola, N., Davies, P.F., Pritchard, W.F., Florez, L., Harbeck, N., Polacek, D.C., 1999. Spatial and temporal regulation of gap junction connexin43 in vascular endothelial cells exposed to controlled disturbed flows in vitro. Proc. Natl. Acad. Sci. 96, 3154–3159.
DePaola, N., Gimbrone, M.A., Davies, P.F., Dewey, C.F., 1992. Vascular endothelium responds to fluid shear stress gradients. Arterioscler. Thromb. Vasc. Biol. 12, 1254–1257.
Dyverfeldt, P., Bissell, M., Barker, A.J., Bolger, A.F., Carlhäll, C.-J., Ebbers, T., Francios, C.J., Frydrychowicz, A., Geiger, J., Giese, D., 2015. 4D flow cardiovascular magnetic resonance consensus statement. J. Cardiovasc. Magn. Reson. 17, 72.
Emory, M., Iaccarino, G., 2014. Visualizing turbulence anisotropy in the spatial domain with componentality contours. Cent. Turbul. Res. Annu. Res. Briefs, 123–138.
Flaherty, J.T., Pierce, J.E., Ferrans, V.J., Patel, D.J., Tucker, W.K., Fry, D.L., 1972. Endothelial nuclear patterns in the canine arterial tree with particular reference to hemodynamic events. Circ. Res. 30, 23–33.
Fry, D.L., 1968. Acute vascular endothelial changes associated with increased blood velocity gradients. Circ. Res. 22, 165–197.
Gimbrone, M.A., García-Cardeña, G., 2016. Endothelial cell dysfunction and the pathobiology of atherosclerosis. Circ. Res. 118, 620–636.
Gårdhagen, R., Lantz, J., Carlsson, F., Karlsson, M., 2010. Quantifying turbulent wall shear stress in a stenosed pipe using large eddy simulation. J. Biomech. Eng. 132, 061002.
Ha, H., Lantz, J., Haraldsson, H., Casas, B., Ziegler, M., Karlsson, M., Saloner, D., Dyverfeldt, P., Ebbers, T., 2016. Assessment of turbulent viscous stress using ICOSA 4D Flow MRI for prediction of hemodynamic blood damage. Sci. Rep. 6.
Ha, H., Lantz, J., Ziegler, M., Casas, B., Karlsson, M., Dyverfeldt, P., Ebbers, T., 2017. Estimating the irreversible pressure drop across a stenosis by quantifying turbulence production using 4D Flow MRI. Sci. Rep. 7.
Ha, H., Ziegler, M., Welander, M., Bjarnegård, N., Carlhäll, C.-J., Lindenberger, M., Länne, T.D.T., Ebbers, T., Dyverfeldt, P., 2018. Age-related vascular changes affect turbulence in the aortic blood flow. Front. Physiol. 9, 36.
Haraldsson, H., Kefa, Kefayati, S., Casas Garcia, B., Lantz, J., Ebbers, T., Saloner, D., 2015. Improved full turbulence tensor quantification using ICOSA6 flow encoding for phase-contrast MRI. In: ISMRM 23rd Annual Meeting and Exhibition 2015. Toronto.
Heiberg, E., Sjögren, J., Ugander, M., Carlsson, M., Engblom, H., Arheden, H., 2010. Design and validation of Segment-freely available software for cardiovascular image analysis. BMC Med. Imaging 10, 1.
Kefayati, S., Haraldsson, H., Casas Garcia, B., Lantz, J., Ebbers, T., Saloner, D., 2015. Application of full turbulent tensor in estimation of MR-based relative pressure. ISMRM 23rd Annual Meeting and Exhibition 2015 Toronto.

Khalifa, A., Giddens, D., 1981. Characterization and evolution of poststenotic flow disturbances. J. Biomech. 14, 279–296.
Khan, M., Valen-Sendstad, K., Steinman, D., 2018. Direct numerical simulation of laminar-turbulent transition in a non-axisymmetric stenosis model for newtonian vs. shear-thinning non-newtonian rheologies. Flow Turbul. Combust., 1–30
Khan, M.O., Chnafa, C., Gallo, D., Molinari, F., Morbiducci, U., Steinman, D.A., Valen-Sendstad, K., 2017. On the quantification and visualization of transient periodic instabilities in pulsatile flows. J. Biomech. 52, 179–182.
Ku, D.N., Giddens, D.P., Zarins, C.K., Glagov, S., 1985. Pulsatile flow and atherosclerosis in the human carotid bifurcation. Positive correlation between plaque location and low oscillating shear stress. Arteriosclerosis: An Off. J. Am. Heart Assoc. Inc. 5, 293–302.
Kwak, B.R., Bäck, M., Bochaton-Piallat, M.-L., Caligiuri, G., Daemen, M.J., Davies, P.F., Hoefer, I.E., Holvoet, P., Jo, H., Krams, R., 2014. Biomechanical factors in atherosclerosis: mechanisms and clinical implications. Eur. Heart J. 35, 3013–3020.
Lantz, J., Ebbers, T., Engvall, J., Karlsson, M., 2013. Numerical and experimental assessment of turbulent kinetic energy in an aortic coarctation. J. Biomech. 46, 1851–1858.
Lantz, J., Gårdhagen, R., Karlsson, M., 2012. Quantifying turbulent wall shear stress in a subject specific human aorta using large eddy simulation. Med. Eng. Phys. 34, 1139–1148.
Lee, S.-W., Antiga, L., Steinman, D.A., 2009. Correlations among indicators of disturbed flow at the normal carotid bifurcation. J. Biomech. Eng. 131, 061013.
Lee, S.E., Lee, S.-W., Fischer, P.F., Bassiouny, H.S., Loth, F., 2008. Direct numerical simulation of transitional flow in a stenosed carotid bifurcation. J. Biomech. 41, 2551–2561.
Liu, K., Pletcher, R.H., 2008. Anisotropy of a turbulent boundary layer. J. Turbul., N18
Lumley, J.L., Newman, G.R., 1977. The return to isotropy of homogeneous turbulence. J. Fluid Mech. 82, 161–178.
Manna, M., Vacca, A., Verzicco, R., 2012. Pulsating pipe flow with large-amplitude oscillations in the very high frequency regime. Part 1. Time-averaged analysis. J. Fluid Mech. 700, 246–282.
Manna, M., Vacca, A., Verzicco, R., 2015. Pulsating pipe flow with large-amplitude oscillations in the very high frequency regime. Part 2. Phase-averaged analysis. J. Fluid Mech. 766, 272–296.
McCormick, S.M., Seil, J.T., Smith, D.S., Tan, F., Loth, F., 2012. Transitional flow in a cylindrical flow chamber for studies at the cellular level. Cardiovasc. Eng. Technol. 3, 439–449.
Morbiducci, U., Gallo, D., Cristofanelli, S., Ponzini, R., Deriu, M.A., Rizzo, G., Steinman, D.A., 2015. A rational approach to defining principal axes of multidirectional wall shear stress in realistic vascular geometries, with application to the study of the influence of helical flow on wall shear stress directionality in aorta. J. Biomech. 48, 899–906.
Morbiducci, U., Ponzini, R., Rizzo, G., Cadioli, M., Esposito, A., Montevecchi, F.M., Redaelli, A., 2011. Mechanistic insight into the physiological relevance of helical blood flow in the human aorta: an in vivo study. Biomech. Model. Mechanobiol. 10, 339–355.
Nicoud, F., Ducros, F., 1999. Subgrid-scale stress modelling based on the square of the velocity gradient tensor. Flow, Turbul. Combust. 62, 183–200.
Noris, M., Morigi, M., Donadelli, R., Aiello, S., Foppolo, M., Todeschini, M., Orisio, S., Remuzzi, G., Remuzzi, A., 1995. Nitric oxide synthesis by cultured endothelial cells is modulated by flow conditions. Circ. Res. 76, 536–543.
Peiffer, V., Sherwin, S.J., Weinberg, P.D., 2013. Computation in the rabbit aorta of a new metric–the transverse wall shear stress–to quantify the multidirectional character of disturbed blood flow. J. Biomech. 46, 2651–2658.
Petersson, S., Dyverfeldt, P., Ebbers, T., 2012. Assessment of the accuracy of MRI wall shear stress estimation using numerical simulations. J. Magn. Reson. Imaging 36, 128–138.
Piatti, F., Pirola, S., Bissell, M., Nesteruk, I., Sturla, F., Della Corte, A., Redaelli, A., Votta, E., 2017. Towards the improved quantification of in vivo abnormal wall shear stresses in BAV-affected patients from 4D-flow imaging: benchmarking and application to real data. J. Biomech. 50, 93–101.
Pope, S.B., 2001. Turbulent Flows. IOP Publishing.
Potters, W.V., Marquering, H.A., VanBavel, E., Nederveen, A.J., 2014. Measuring wall shear stress using velocity-encoded MRI. Curr. Cardiovasc. Imaging Rep. 7, 9257.
Potters, W.V., Ooij, P., Marquering, H., vanBavel, E., Nederveen, A.J., 2015. Volumetric arterial wall shear stress calculation based on cine phase contrast MRI. J. Magn. Reson. Imaging 41, 505–516.
Rowland, E.M., Mohamied, Y., Chooi, K.Y., Bailey, E.L., Weinberg, P.D., 2015. Comparison of statistical methods for assessing spatial correlations between maps of different arterial properties. J. Biomech. Eng. 137, 101003.
Valen-Sendstad, K., Mardal, K.-A., Steinman, D.A., 2013. High-resolution CFD detects high-frequency velocity fluctuations in bifurcation, but not sidewall, aneurysms. J. Biomech. 46, 402–407.
Valen-Sendstad, K., Piccinelli, M., Steinman, D.A., 2014. High-resolution computational fluid dynamics detects flow instabilities in the carotid siphon: implications for aneurysm initiation and rupture? J. Biomech. 47, 3210–3216.
Wang, L., Luo, J.-Y., Li, B., Tian, X.Y., Chen, L.-J., Huang, Y., Liu, J., Deng, D., Lau, C.W., Wan, S., 2016. Integrin-YAP/TAZ-JNK cascade mediates atheroprotective effect of unidirectional shear flow. Nature 540, 579–582.
Varghese, S.S., Frankel, S.H., Fischer, P.F., 2007. Direct numerical simulation of stenotic flows. Part 2. Pulsatile flow. J. Fluid Mech. 582, 281–318.
Zajac, J., Eriksson, J., Dyverfeldt, P., Bolger, A.F., Ebbers, T., Carlhäll, C.J., 2015. Turbulent kinetic energy in normal and myopathic left ventricles. J. Magn. Reson. Imaging 41, 1021–1029.
Ziegler, M., Lantz, J., Ebbers, T., Dyverfeldt, P., 2017. Assessment of turbulent flow effects on the vessel wall using four-dimensional flow MRI. Magn. Reson. Med. 77, 2310–2319.